Atomic Resolution in Near-Edge Core-Loss Mapping Beyond the Conventional Delocalization Limit

Jiayi Wu[1], Juri Barthel[2], Leslie J. Allen[3] and Mitsutaka Haruta[1,*]

[1]*Institute for Chemical Research, Kyoto University, Kyoto 611-0011, Japan*

[2]*Ernst Ruska-Centre (ER-C 2), Forschungszentrum Jülich GmbH, Jülich 52428, Germany*

[3]*School of Physics, University of Melbourne, Parkville, Victoria 3010, Australia*

The spatial resolution of core-loss electron energy-loss spectroscopy (EELS) is limited by the delocalization of inelastic scattering from long-range Coulomb interactions, especially for light-element edges at low energy-losses. Here we demonstrate atomic-resolution imaging of the Si *L*-edge in Si [110] using dark-field annular EELS (DF-AEELS) that selectively detects high-angle inelastic scattering. Although the intrinsic excitation delocalization remains unchanged, momentum-transfer–selective detection suppresses long-range contributions, enabling the 1.36 Å Si dumbbell to be resolved.

Atomic-scale characterization of electronic states is essential for understanding chemical bonding and emergent material functionality. Electron energy-loss spectroscopy (EELS) combined with aberration-corrected scanning transmission electron microscopy (STEM) provides access to elemental and electronic-structure information with atomic resolution [1-3]. However, unlike elastic imaging, the spatial resolution of core-loss EELS has long been known to be fundamentally limited by the delocalization of inelastic scattering [1,4-11]. Although the interaction is mediated by the long-range Coulomb potential, the effective spatial extent of a core-loss excitation is determined by the transition matrix element, that is, by the spatial overlap between the localized initial core state and the continuum final state of the excited electron. Consequently, the effective interaction range is governed by the energy-dependent momentum transfer associated with the excitation process. This intrinsic limitation is commonly estimated by the delocalization length, defined as the radius containing half of the excitation intensity [12],

$$d_{50} \simeq 0.5\lambda/(\frac{\Delta E}{2E_0})^{\frac{3}{4}} \quad , \qquad (1)$$

where λ is the wavelength, E_0 is the incident energy and ΔE is the energy-loss in the inelastic interaction. This approximation is in reasonable agreement with experiments [5,10,13]. The scaling predicts that strong spatial spreading for low-energy excitations, usually the case for light element edges, should preclude atomic resolution in conventional STEM-EELS. This limitation is particularly critical for achieving high spatial resolution in energy-loss near-edge structure (ELNES) spectroscopic imaging, typically within ~50 eV above the edge onset, which reflects the local unoccupied density of states and provides direct information on chemical bonding. Accessing atomic-resolution imaging in the ELNES energy range has therefore remained a central challenge of core-loss EELS. For example, for the Si *L* edge (~100 eV), the estimated delocalization length at an incident energy of 200 kV is ~5.6 Å, significantly exceeding the 1.36 Å atomic spacing of the Si [110] dumbbell projection. Under such conditions, EELS maps are expected to reflect mixed excitation probabilities from neighboring atomic columns rather than true atomic localization[14-16] and even exhibit contrast loss or reversal depending on specimen thickness [13,17]. In practice, measured contrast is further modified by signal mixing arising from electron channeling in specimens of finite thickness. Inversion approaches have been developed to remove such channeling-induced mixing, but they require prior structural knowledge and do not alter the intrinsic spatial extent of the inelastic interaction itself [18-20]. Atomic-resolution energy-filtered (EF-) TEM imaging of the Si *L*-edge has also been demonstrated using Cs/Cc-corrected EF-TEM [21]. However, the atomic contrast in EF-TEM was attributed mainly to preserved elastic contrast, including elastic channeling before and after ionization. In addition to this strong intermixing of elastic and inelastic scattering, the limited energy resolution in EFTEM is not helpful for

exploring the ELNES region with high spatial resolution.

An approach using STEM has been proposed to mitigate delocalization through selective detection of inelastic scattering. Off-axis (dark-field) EELS geometries [22,23] achieve single-atom vibrational spectroscopy by detecting only a subset of the high-angle inelastic scattering. In vibrational EELS, localization enhancement is often associated with suppression of long-range dipole scattering and increasing relative contributions from short-range impact scattering. Annular EELS (AEELS) [7,24] should allow us to more efficiently collect core-loss electrons scattered over a large angular range while suppressing low-angle contributions associated with long-range excitations. Despite this expectation, earlier AEELS experiments reported only modest improvements in spatial resolution[25]. While the conventional delocalization limit for EELS implicitly assumes momentum-integrated detection of inelastic scattering, selective detection in momentum-transfer space should provide a pathway to improve upon the fundamental limit in Eq. (1).

Here we demonstrate the circumvention of this long-standing experimental barrier. By combining dark-field annular EELS (DF-AEELS), in which the central direct beam is fully excluded, with a multi-frame spectrum-imaging acquisition strategy [26-28] that restores detection efficiency, we achieve atomic-resolution mapping of the Si *L*-edge in the [110] projection of crystalline silicon. These results demonstrate that the widely accepted delocalization-based resolution limit of core-loss EELS is not general but depends critically on the momentum space sampled in detection. Momentum-selective DF-AEELS therefore enables atomic-scale measurements in energy regimes usually regarded as fundamentally resolution-limited.

Samples were prepared by crushing a silicon single crystal. Each specimen was oriented in [110] projection in the microscope. STEM–EELS experiments were performed at 200 kV accelerating voltage using an aberration-corrected microscope (JEOL ARM-200F) with a probe convergence semi-angle of α = 24.6 mrad. Conventional EELS (CEELS) measurements employed a collection semi-angle range of β = 0–75.4 mrad, whereas DF-AEELS measurements selectively detected high-angle inelastic scattering using an annular collection range of β = 32.3–75.4 mrad (corresponding to transverse component of scattering-vector range of $q_\perp$ = 8.1 – 18.9 Å^{-1}). In the annular configuration, the beam stop fully excluded the direct beam, realizing the DF-AEELS condition illustrated in Fig. 1(a). HAADF images were acquired simultaneously with a detector range of 75.4–150.8 mrad. The

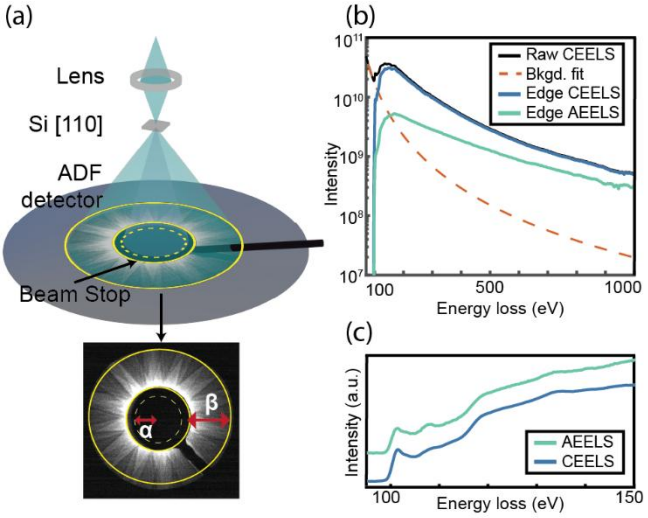

FIG. 1. (a) Experimental setup of DF-AEELS. The beam stop fully blocks the direct beam, which has a convergence angle α = 24.6 mrad. The range of collection angles β = 32.3-75.4 mrad. The solid circles indicate the inner and outer collection angle for DF-AEELS, and the dashed circle indicates the direct beam; (b) Typical spectrum for CEELS and AEELS, both normalized to the same exposure time. Both spectra were processed with a power-law background subtraction. (c) Typical Si *L*-edge ELNES for CEELS and AEELS.

dwell times of the low-loss and core-loss sectors were ~0.1 ms and ~4 ms per pixel, respectively, with an energy dispersion of 0.5 eV/channel. Ultra-high quality dark reference subtraction was used [29]. All Si *L*-edge maps were obtained by integrating the signal over 25-eV wide energy-loss windows.

Figure 1(b) shows that the Si *L*-edge signal obtained under AEELS conditions is substantially weaker than in CEELS, reflecting the exclusion of low-angle inelastic scattering. In the near-edge region, the annular signal is approximately one order of magnitude lower than CEELS, while becoming comparable at higher energy losses (~500 eV). The corresponding ELNES spectra [Fig. 1(c)], measured with an energy dispersion of 0.1 eV/channel, clearly exhibit angular-dependent variations consistent with momentum-selective detection. To recover counting statistics without altering spatial information, multi-frame acquisition and template matching (using 2000-6000 motifs) were applied, adjusting specimen drift using non-rigid registration with the HREM package SmartAlign [26-28,30]. Thickness-dependent measurements were performed for three ranges (300–500 Å, 900–1100 Å, and 1400–1600 Å), determined using the EELS log-ratio method [12].

STEM-EELS calculations were performed using the

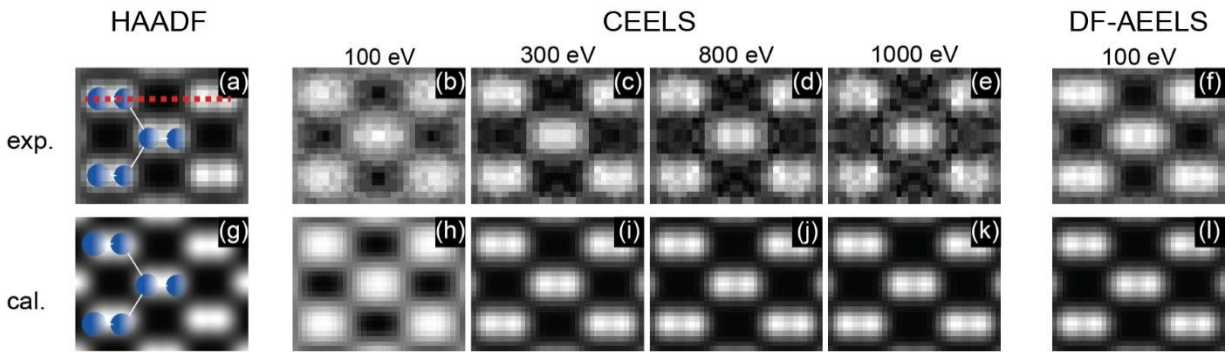

FIG. 2. Experimental and calculated HAADF and Si L-edge maps at ~400 Å thickness. All Si L-edge maps are integrated over a 25-eV energy window, and the indicated energy-loss value marks the lower bound of that window. The image contrast of each panel was individually adjusted for clarity.

multi-slice method as implemented in μSTEM (version 6.3) [31,32], assuming an aberration-free probe. The calculation parameters were set to resemble the experimental conditions. Inelastic transitions with a change of the orbital angular momentum up to $\Delta l = \pm 1$ were included. The effect of thermal vibrations was simulated by applying the quantum excitation of phonons (QEP) model [33] and included propagation of inelastic wave functions after ionization through the remaining crystal before detection, i.e., so-called double channeling [34]. A Si crystal structure model was used with a lattice constant of 5.43 Å and an atomic mean-squared displacement $U = 0.0059$ Å^2. Calculated maps were convolved with a Gaussian of ~1.2 Å (FWHM) to account for the effective source size [35]. Due to substantial computational costs, the calculations were only performed up to 500 Å sample thickness.

Figure 2 compares the experimental HAADF and Si L-edge maps acquired from a specimen of ~400 Å thickness with corresponding calculations. The HAADF image [shown in Fig. 2(a)] clearly resolves the dumbbell structure of the Si atomic columns, which are separated by 1.36 Å, and there is a good match with the calculation [Fig. 2(g)], confirming that the probe size is sufficient to resolve the projected atomic columns. The CEELS maps in Figs. 2(b)-(e) reveal a systematic evolution of spatial resolution with increasing energy loss. In the near-edge region [100–125 eV interval shown in Fig. 2(b)], where Eq. (1) predicts a delocalization length of $d_{50} \approx 5.6$ Å, the Si dumbbell structure was not resolved despite sufficient SNR [17]. With increasing energy loss [Figs. 2(c)-(e)], the atomic columns become progressively more separated, showing evidence for a reduction in delocalization and a corresponding enhancement in spatial resolution. Based on Rayleigh's criterion for a 1D profile ($I/I_{\max} < 0.811$, where I is the minimum intensity at the interatomic dip in the dumbbell and $I_{\max}$ represents the peak intensity) [36], the dumbbell structure can be regarded as resolved in the 800-825 eV energy-loss range, where $d_{50}^{800eV} \approx 1.3$ Å. Figures 2(h)-(k) are the corresponding calculated images, reproducing the spatial resolution enhancement with higher energy loss.

Having reproduced the conventional energy-dependent resolution limit, we next examine the momentum-selective detection. Under the DF-AEELS condition (β = 32.3–75.4 mrad), where the direct beam is completely excluded, the Si dumbbells are clearly resolved for the 100-125 eV energy-loss window [Fig. 2(f)]. This result demonstrates that atomic resolution can be recovered without increasing energy loss, indicating that the apparent delocalization limit depends on the sampled momentum-transfer range rather than solely on the intrinsic excitation process. The calculation shown in Fig. 2(l) reproduces the observed enhancement.

To quantify the resolution enhancement, we compare normalized intensity line profiles obtained under identical probe conditions. Figure 3(a) shows the observed improvement of spatial resolution in CEELS with increasing energy loss, reflecting the reduction of delocalization expected according to Eq. (1). Remarkably, the DF-AEELS

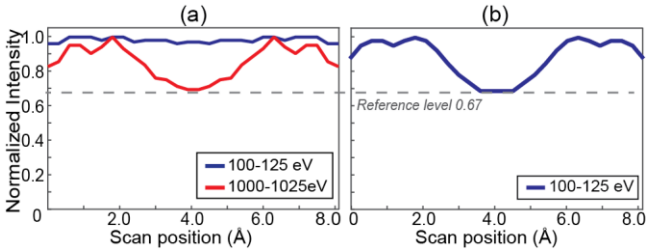

FIG. 3. Normalized line profiles of Si L-edge maps for a ~400 Å-thick sample for: (a) CEELS and (b) DF-AEELS. The dotted line in Fig. 2(a) marks the scan path.

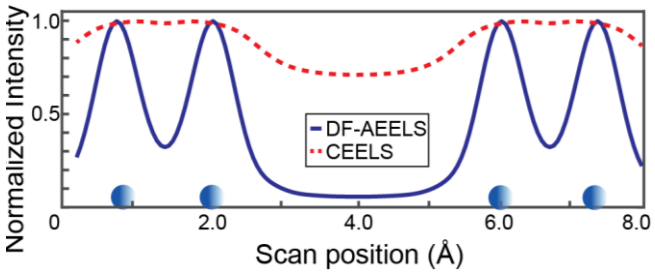

FIG. 4. Calculated mono-layer Si [110] line profiles comparison between DF-AEELS and CEELS without Gaussian convolution. The spheres indicate the position of Si atomic columns.

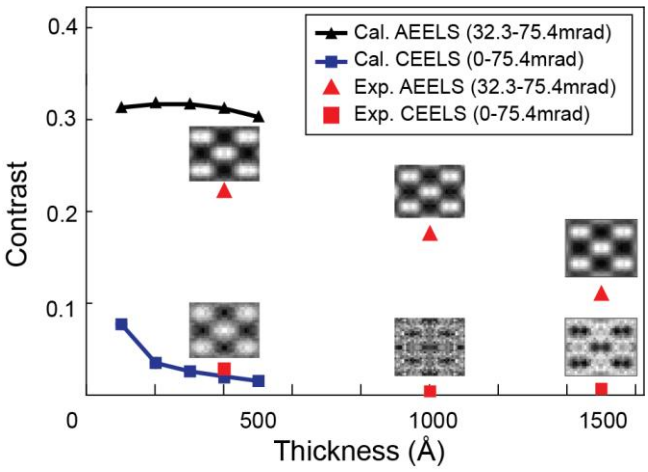

FIG. 5. Image contrast of DF-AEELS and CEELS as a function of thickness. Calculations were carried out using the QEP model including double channeling. Insets display experimental Si *L*-edge maps (100-125 eV) at the corresponding thicknesses; each contrast were individually adjusted for clarity.

profiles in the near-edge region [Fig. 3(b)] exhibits substantially improved contrast. The CEELS profiles at 1000–1025 eV ($d_{50}^{1000eV} \approx 1.0$ Å) closely match those obtained by DF-AEELS at β = 32.3–75.4 mrad. The minimum intensity between the Si dumbbells decreases to 0.67 for the annular range. This indicates that selective detection of large-angle scattering filters the signal arising from the excitation process, preferentially retaining the more localized components. Furthermore, DF-AEELS produces an effective spatial localization comparable to that achieved in conventional EELS only at substantially higher energy losses. While multiple scattering in thick specimens inevitably mixes signals from neighboring atomic columns, the observed correspondence confirms that the effective delocalization length is governed by the sampled momentum-transfer range rather than solely by excitation energy.

To isolate the intrinsic excitation mechanism from probe and multiple-scattering effects, we analyzed calculated monolayer Si *L*-edge maps without Gaussian convolution. Figure 4 shows normalized intensity line profiles across the Si dumbbells in the calculated Si *L*-edge maps of CEELS and DF-AEELS conditions. In this idealized limit, the CEELS profile exhibits substantial intensity both between and within the dumbbells, reflecting the long-range character of inelastic scattering. In contrast, the DF-AEELS profile shows a pronounced suppression of intensity away from atomic columns. This direct comparison demonstrates that selecting only large-angle inelastically scattered electrons effectively removes long-range (delocalized) contributions, enhancing the apparent spatial resolution in the Si *L*-edge mapping.

The robustness of the resolution enhancement against specimen thickness is summarized in Fig. 5, which plots the Michelson fringe visibility $C = (I_{\max} - I_{\min})/(I_{\max} + I_{\min})$ [25] as a function of thickness. In CEELS, the image contrast rapidly decreases with increasing thickness and approaches zero, accompanied by the well-known contrast reversal in the near-edge region for thick specimens (as the inset corresponding to ~1500 Å thickness), consistent with previous reports [13]. In contrast, DF-AEELS maintains substantial contrast and preserves the positive dumbbell contrast without reversal over a wide thickness range, with only a gradual reduction as thickness increases. These results demonstrate that momentum-selective detection stabilizes projected atomic contrast against multiple scattering, enabling atomic-scale imaging even in comparatively thick specimens.

In summary, we demonstrate experimentally that the commonly assumed spatial-resolution limitation of core-loss STEM-EELS, arising from inelastic delocalization, does not universally determine the achievable atomic contrast. While the intrinsic spatial extent of the ionization process remains unchanged, momentum-transfer–selective detection in DF-AEELS suppresses long-range scattering contributions and stabilizes projected atomic contrast over a wide range of specimen thicknesses without contrast reversal. As a result, atomic-resolution mapping of the Si *L*-edge near edge region in the Si [110] projection, which was previously strongly limited by delocalization, becomes experimentally accessible. The observed improvement originates from preferential detection of high-angle inelastic scattering. These results suggest that future formulations of delocalization-limited spatial resolution in STEM-EELS should incorporate not only the intrinsic excitation process, but also the momentum-transfer selectivity introduced by the detection geometry.

ELNES spectra acquired at large scattering angles may

contain additional electronic-structure information beyond dipole-dominated transitions [37], motivating future investigations of angular-dependent fine structure. Improving the effective spatial resolution in the ELNES regime is expected to enhance atomic-scale mapping of electronic structure [38,39] and orbital anisotropy [40-43]. In particular, momentum-selective detection may provide a pathway toward more localized measurements of bonding-sensitive fine structure and angular-dependent transitions. In addition, extending DF-AEELS to other light-element edges, such as Li, opens a pathway toward chemically sensitive atomic-scale analysis in materials where low-energy core excitations have long been regarded as intrinsically resolution-limited. Practically, together with continued improvements in detector performance and automated acquisition, DF-AEELS can become applicable to localized measurements and point spectroscopy even for beam-sensitive light-element systems.

Acknowledgement—This work was supported by Kyoto University Research Development Program (ISHIZUE). The data that supports the findings of this study are not publicly available upon publication because it is not technically feasible and/or the cost of preparing, depositing, and hosting the data would be prohibitive within the terms of this research project. Experimental and calculated data was generated at Kyoto University and Ernst Ruska-Centre, respectively. Derived data supporting the findings of this study are available from the corresponding author, M. Haruta, upon reasonable request.

[1] K. Kimoto, T. Asaka, T. Nagai, M. Saito, Y. Matsui, and K. Ishizuka, Nature 450, 702 (2007).
[2] M. Bosman, V. J. Keast, J. L. Garcia-Munoz, A. J. D'Alfonso, S. D. Findlay, and L. J. Allen, Phys. Rev. Lett. 99, 086102 (2007).
[3] D. A. Muller, L. F. Kourkoutis, M. M., J. H. Song, H. Y. Hwang, J. Silcox, N. Dellby, and O. L. Krivanek, Science 319, 1073 (2008).
[4] L. J. Allen, Ultramicroscopy 48, 97 (1993).
[5] D. A. Muller and J. Silcox, Ultramicroscopy (1995).
[6] M. P. Oxley and L. J. Allen, Phys. Rev. B 57, 3273 (1998).
[7] B. Rafferty and S. J. Pennycook, Ultramicroscopy 78, 141 (1999).
[8] M. P. Oxley and L. J. Allen, Ultramicroscopy 80, 125 (1999).
[9] E. C. Cosgriff, M. P. Oxley, L. J. Allen, and S. J. Pennycook, Ultramicroscopy 102, 317 (2005).
[10] R. F. Egerton, Ultramicroscopy 107, 575 (2007).
[11] R. F. Egerton, Ultramicroscopy 180, 115 (2017).
[12] R. F. Egerton, in Electron Energy-Loss Spectroscopy in the Electron Microscope (Springer US, Boston, MA, 2011), pp. 293.
[13] P. Wang, A. J. D'Alfonso, S. D. Findlay, L. J. Allen, and A. L. Bleloch, Phys. Rev. Lett. 101, 236102 (2008).
[14] M. Haruta, H. Kurata, H. Komatsu, Y. Shimakawa, and S. Isoda, Phys. Rev. B 80, 165123 (2009).
[15] B. D. Forbes, A. J. D'Alfonso, R. E. A. Williams, R. Srinivasan, H. L. Fraser, D. W. McComb, B. Freitag, D. O. Klenov, and L. J. Allen, Phys. Rev. B 86, 024108 (2012).
[16] M. Haruta, H. Higuchi, T. Nemoto, and H. Kurata, Appl. Phys. Lett. 113 (2018).
[17] H. Tan, Y. Zhu, C. Dwyer, and H. L. Xin, Phys. Rev. B 90 (2014).
[18] N. R. Lugg, M. Haruta, M. J. Neish, S. D. Findlay, T. Mizoguchi, K. Kimoto, and L. J. Allen, Appl. Phys. Lett. 101 (2012).
[19] M. J. Neish, N. R. Lugg, S. D. Findlay, M. Haruta, K. Kimoto, and L. J. Allen, Phys. Rev. B 88, 115120 (2013).
[20] M. Haruta, T. Nagai, N. R. Lugg, M. J. Neish, M. Nagao, K. Kurashima, L. J. Allen, T. Mizoguchi, and K. Kimoto, J. Appl. Phys. 114 (2013).
[21] K. W. Urban, J. Mayer, J. R. Jinschek, M. J. Neish, N. R. Lugg, and L. J. Allen, Phys. Rev. Lett. 110, 185507 (2013).
[22] F. S. Hage, D. M. Kepaptsoglou, Q. M. Ramasse, and L. J. Allen, Phys. Rev. Lett. 122, 016103 (2019).
[23] F. S. Hage, G. Radtke, D. M. Kepaptsoglou, M. Lazzeri, and Q. M. Ramasse, Science 367, 1124 (2020).
[24] C. Dwyer, Phys. Rev. B 89 (2014).
[25] G. Ruben, M. Bosman, A. J. D'Alfonso, E. Okunishi, Y. Kondo, and L. J. Allen, Ultramicroscopy 111, 1540 (2011).
[26] L. Jones, H. Yang, T. J. Pennycook, M. S. J. Marshall, S. Van Aert, N. D. Browning, M. R. Castell, and P. D. Nellist, Adv. Struct. Chem. Imag. 1, 16, 8 (2015).
[27] L. Jones et al., Microscopy 67, i98 (2018).
[28] M. Haruta, Y. Fujiyoshi, T. Nemoto, A. Ishizuka, K. Ishizuka, and H. Kurata, Phys. Rev. B 97, 205139 (2018).
[29] M. Haruta, Y. Fujiyoshi, T. Nemoto, A. Ishizuka, K. Ishizuka, and H. Kurata, Ultramicroscopy 207, 112827 (2019).
[30] M. Bosman and V. J. Keast, Ultramicroscopy 108, 837 (2008).
[31] L. J. Allen, A. J. D'Alfonso, and S. D. Findlay, Ultramicroscopy 151, 11 (2015).
[32] μSTEM (Version 6.3), (Barthel, J.)

https://github.com/ju-bar/MuSTEM (2025).
[33] B. D. Forbes, A. V. Martin, S. D. Findlay, A. J. D'Alfonso, and L. J. Allen, Phys. Rev. B 82, 104103 (2010).
[34] L. J. Allen, S. D. Findlay, M. P. Oxley, C. Witte, and N. J. Zaluzec, Phys. Rev. B 73, 094104 (2006).
[35] C. Dwyer, R. Erni, and J. Etheridge, Ultramicroscopy 110, 952 (2010).
[36] M. Born and E. Wolf, Principles of Optics: Electromagnetic Theory of Propagation, Interference and Diffraction of Light (Cambridge University Press, Cambridge, 1999), 7 edn.
[37] S. Löffler, I. Ennen, F. Tian, P. Schattschneider, and N. Jaouen, Ultramicroscopy 111, 1163 (2011).
[38] H. Tan, S. Turner, E. Yücelen, J. Verbeeck, and G. Van Tendeloo, Phys. Rev. Lett. 107, 107602 (2011).
[39] M. Haruta, K. Kurashima, T. Nagai, H. Komatsu, Y. Shimakawa, H. Kurata, and K. Kimoto, Appl. Phys. Lett. 100 (2012).
[40] M. Bugnet, M. Ederer, V. K. Lazarov, L. Li, Q. M. Ramasse, S. Löffler, and D. M. Kepaptsoglou, Phys. Rev. Lett. 128, 116401 (2022).
[41] C. Iwashimizu, M. Haruta, T. Nemoto, and H. Kurata, Microscopy 72, 353 (2023).
[42] M. Bugnet, S. Löffler, M. Ederer, D. M. Kepaptsoglou, and Q. M. Ramasse, J. Microsc. 295, 217 (2024).
[43] C. Iwashimizu, M. Haruta, and H. Kurata, Physical Review B 111, 155147 (2025).